

Spin Dynamics in Hierarchical Black Hole Triples: Predicting Final Spin-Orbit Misalignment Angle From Initial Conditions

YUBO SU,¹ DONG LAI,¹ AND BIN LIU¹

¹*Cornell Center for Astrophysics and Planetary Science, Department of Astronomy, Cornell University, Ithaca, NY 14853, USA*

(Received XXXX; Revised XXXX; Accepted XXXX)

Submitted to ApJL

ABSTRACT

Abstract

Keywords: keywords

1. INTRODUCTION

We study the so-called dynamical formation channel of BH binaries, where dynamical processes bring widely separated BHs into sufficiently close orbits to allow their coalescence to be driven by gravitational radiation.

It is well known that a tertiary body on an inclined orbit can accelerate the orbital decay of an inner binary by inducing Lidov-Kozai (LK) oscillations in eccentricity and inclination (Kozai 1962; Lidov 1962).

In previous works, we studied two qualitatively different scenarios for dynamical BH binary formation: (i) in Liu & Lai (2017), we studied what we here call “mildly LK-enhanced mergers”, where LK oscillations accelerate the coalescence of a binary that would normally merge within a Hubble time; and (ii) in Liu & Lai (2018), we studied what we here call “LK-induced mergers”, where LK oscillations enable the coalescence of binaries whose merger time in isolation far exceeds a Hubble time. In both of these papers, we analyzed the dynamics of the angle θ_{sl}^f , defined as the misalignment angle between the spin of one BH and the angular momentum axis of the binary at merger. The distribution of θ_{sl}^f is of interest as it is both measurable and disambiguates between BH binaries forming via isolated and dynamical channels.

In particular, consider the Figs. 1 and 2, generated for parameters from Liu & Lai (2017) and Liu & Lai (2018) respectively. Interestingly, the two plots show very different behavior for θ_{sl}^f . However, it is prohibitive to numerically explore the θ_{sl}^f distribution for the entire parameter space of dynamically-formed BH binaries. Instead, in this work we

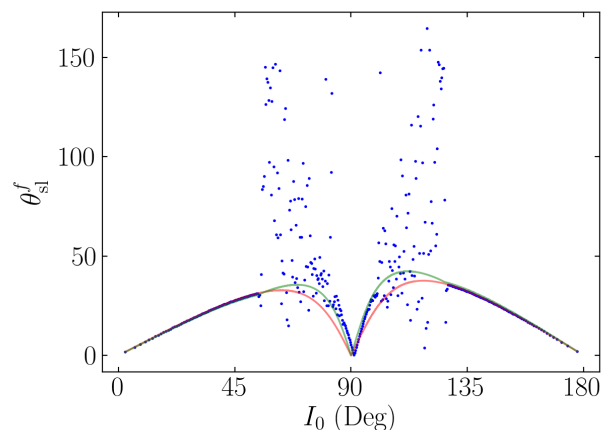


Figure 1. Plot of θ_{sl}^f for $m_1 = m_2 = m_3 = 30M_{\odot}$, $a_{\text{in}} = 0.1$ AU, $\tilde{a}_3 = 3$ AU, $e_3 = 0$, where $e_0 = 0.001$ and $\theta_{\text{sl}}^i = 0$ over a restricted range of I_0 (analogous to the top panel of Fig. 4 in Liu & Lai 2017). The blue dots denote θ_{sl}^f obtained from numerical simulation. The red line denotes the θ_{sl}^f prediction made in Liu & Lai (2017), which has the wrong scaling near $I_0 = 90^\circ$ and does not explain the large deviations for $I_0 \lesssim 80^\circ$ and $I_0 > 100^\circ$. Corresponds to top panel of Fig. 4 of Liu & Lai (2017).

develop an analytical understanding of the processes shaping θ_{sl}^f in a general manner.

In Section 2, we set up the relevant equations of motion for the orbital and spin evolution of the three BHs, and we argue for the primary result of the paper, conservation of the angle θ_e . In Sections 3 and 4, we consider two scenarios under which conservation of θ_e can be violated. We discuss and conclude in Section 5.

2. ANALYTICAL SETUP

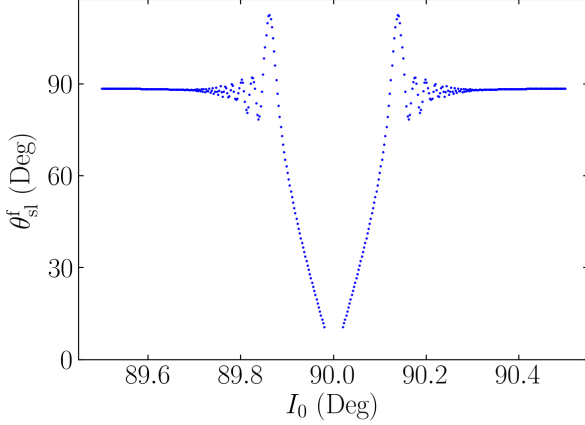


Figure 2. Plot of θ_{sl}^f for $m_1 = 30M_\odot$, $m_2 = 20M_\odot$, $m_3 = 3 \times 10^7 M_\odot$, $a_{\text{in}} = 100$ AU, $\tilde{a}_3 = 2.2$ pc, $e_3 = 0$, where $e_0 = 0.001$ and $\theta_{\text{sl}}^i = 0$ over a restricted range of I_0 (analogous to the bottom-most panel in Fig. 3 of Liu & Lai 2018), where the blue dots are taken from numerical simulations. It is clear that for I_0 sufficiently far from 90° , the resulting θ_{sl}^f are quite similar and are near 90° (Liu & Lai 2018). Bottom panel of Fig. 3 of Liu & Lai (2018).

2.1. Orbital Evolution

We study Lidov-Kozai (LK) oscillations due to an external perturber to quadrupole order and include precession of pericenter and gravitational wave radiation due to general relativity. Consider an black hole (BH) binary with masses m_1 and m_2 having total mass m_{12} and reduced mass μ orbiting a supermassive black hole (SMBH) with mass $m_3 \gg m_1$ and m_2 . Call a_3 and e_3 the semimajor axis and eccentricity of the orbit of the inner binary around the SMBH, and define effective semimajor axis

$$\tilde{a}_3 \equiv a_3 \sqrt{1 - e_3^2}. \quad (1)$$

Finally, call $\mathbf{L}_{\text{out}} \equiv L_{\text{out}} \hat{\mathbf{L}}_{\text{out}}$ the angular momentum of the SMBH relative to the center of mass of the inner BH binary, and call $\mathbf{L} \equiv L \hat{\mathbf{L}}$ the orbital angular momentum of the inner BH binary. We take \mathbf{L}_{out} to be fixed.

We then consider the motion of the inner binary, described by the Keplerian orbital elements $(a, e, \varpi, I, \omega)$ (respectively: semimajor axis, eccentricity, longitude of the ascending node, inclination, and argument of periapsis). The equations describing the motion of these orbital elements are (Peters 1964;

Storch & Lai 2015; Liu & Lai 2018)

$$\frac{da}{dt} = \left(\frac{da}{dt} \right)_{\text{GW}}, \quad (2)$$

$$\frac{de}{dt} = \frac{15}{8t_{\text{LK}}} e \sqrt{1 - e^2} \sin 2\omega \sin^2 I + \left(\frac{de}{dt} \right)_{\text{GW}}, \quad (3)$$

$$\frac{d\varpi}{dt} = \frac{3}{4t_{\text{LK}}} \frac{\cos I (5e^2 \cos^2 \omega - 4e^2 - 1)}{\sqrt{1 - e^2}}, \quad (4)$$

$$\frac{dI}{dt} = \frac{15}{16} \frac{e^2 \sin 2\omega \sin 2I}{\sqrt{1 - e^2}}, \quad (5)$$

$$\frac{d\omega}{dt} = \frac{3}{4t_{\text{LK}}} \frac{2(1 - e^2) + 5 \sin^2 \omega (e^2 - \sin^2 I)}{\sqrt{1 - e^2}} + \Omega_{\text{GR}}, \quad (6)$$

where we define

$$t_{\text{LK}}^{-1} = n \left(\frac{m_3}{m_{12}} \right) \left(\frac{a}{\tilde{a}_3} \right)^3, \quad (7)$$

$$\begin{aligned} \left(\frac{da}{dt} \right)_{\text{GW}} &= -\frac{a}{t_{\text{GW}}}, \\ &= \frac{64}{5} \frac{G^3 \mu m_{12}^2}{c^5 a^3} \frac{1}{(1 - e^2)^{7/2}} \left(1 + \frac{73}{24} e^2 + \frac{37}{96} e^4 \right), \end{aligned} \quad (8)$$

$$\left(\frac{de}{dt} \right)_{\text{GW}} = -\frac{304}{15} \frac{G^3 \mu m_{12}^2}{c^5 a^4} \frac{1}{(1 - e^2)^{5/2}} \left(1 + \frac{121}{304} e^2 \right), \quad (9)$$

$$\Omega_{\text{GR}} = \frac{3Gnm_{12}}{c^2 a (1 - e^2)}, \quad (10)$$

and $n = \sqrt{Gm_{12}/a^3}$ is the mean motion of the inner binary. We will often refer to e_{min} and e_{max} the minimum/maximum eccentricity in a single LK cycle, and we will sometimes notate $j = \sqrt{1 - e^2}$ and $j_{\text{min}} = \sqrt{1 - e_{\text{max}}^2}$.

Finally, for concreteness, we adopt fiducial parameters similar to those from Liu & Lai (2018): the inner binary has $a = 100$ AU, $m_1 = 30M_\odot$, $m_2 = 20M_\odot$, and initial $e_0 = 0.001$ with varying I_0 . We take the SMBH tertiary companion to have $m_3 = 3 \times 10^7 M_\odot$ and $\tilde{a}_3 = 4.5 \times 10^5$ AU = 2.2 pc. This gives the same t_{LK} as in Liu & Lai (2018).

2.2. Spin Dynamics: An Approximate Adiabatic Invariant

We are ultimately interested in the spin orientations of the inner BHs at merger as a function of initial conditions. Since they evolve independently to leading post-Newtonian order, we focus on the dynamics of a single BH spin vector $\mathbf{S} = S \hat{\mathbf{S}}$. Neglecting spin-spin interactions, $\hat{\mathbf{S}}$ undergoes de Sitter precession about \mathbf{L} as

$$\frac{d\hat{\mathbf{S}}}{dt} = \Omega_{\text{SL}} \hat{\mathbf{L}} \times \hat{\mathbf{S}}, \quad (12)$$

$$\Omega_{\text{SL}} = \frac{3Gn(m_2 + \mu/3)}{2c^2 a (1 - e^2)}. \quad (13)$$

To analyze the dynamics of the spin vector, we go to co-rotating frame with $\hat{\mathbf{L}}$ about $\hat{\mathbf{L}}_{\text{out}}$. Choose $\hat{\mathbf{L}}_{\text{out}} = \hat{\mathbf{z}}$, and choose the $\hat{\mathbf{x}}$ axis such that $\hat{\mathbf{L}}$ lies in the x - z plane. In this coordinate system, Eq. (12) becomes

$$\left(\frac{d\hat{\mathbf{S}}}{dt}\right)_{\text{rot}} = \left(-\frac{d\Omega}{dt}\hat{\mathbf{z}} + \Omega_{\text{SL}}\hat{\mathbf{L}}\right) \times \hat{\mathbf{S}}, \quad (14)$$

$$= \boldsymbol{\Omega}_e \times \hat{\mathbf{S}}, \quad (15)$$

$$\boldsymbol{\Omega}_e \equiv \Omega_L \hat{\mathbf{z}} + \Omega_{\text{SL}} (\cos I \hat{\mathbf{z}} + \sin I \hat{\mathbf{x}}), \quad (16)$$

$$\Omega_L \equiv -\frac{d\Omega}{dt}. \quad (17)$$

In general, Eq. (15) is difficult to analyze, since Ω_L , Ω_{SL} and I all vary significantly within each LK period, and we are interested in the final outcome after many LK periods. However, if we assume $t_{\text{GW}} \gg t_{\text{LK}}$, then the system can be treated as nearly periodic within each LK cycle. We can then rewrite Eq. (15) in Fourier components

$$\left(\frac{d\hat{\mathbf{S}}}{dt}\right)_{\text{rot}} = \left[\bar{\boldsymbol{\Omega}}_e + \sum_{N=1}^{\infty} \boldsymbol{\Omega}_{eN} \cos\left(\frac{2\pi Nt}{P_{\text{LK}}}\right)\right] \times \hat{\mathbf{S}}. \quad (18)$$

The bar denotes an average over an LK cycle. We adopt convention where $t = 0$ is the maximum eccentricity phase of the LK cycle.

It is next useful to define inclination angle I_e as the angle between $\bar{\boldsymbol{\Omega}}_e$ and \mathbf{L}_{out} as shown in Fig. 4. I_e can be expressed in closed form. When the eccentricity is strongly oscillatory within each LK cycle (early in the evolution, see Fig. 3), we define averaged quantities

$$\overline{\Omega_{\text{SL}} \sin I} \equiv \bar{\Omega}_{\text{SL}} \sin \bar{I}, \quad (19)$$

$$\overline{\Omega_{\text{SL}} \cos I} \equiv \bar{\Omega}_{\text{SL}} \cos \bar{I}. \quad (20)$$

Then, using Eq.(16), we can see that

$$\tan I_e = \frac{\mathcal{A} \sin \bar{I}}{1 + \mathcal{A} \cos \bar{I}}, \quad (21)$$

where

$$\mathcal{A} \equiv \frac{\bar{\Omega}_{\text{SL}}}{\bar{\Omega}_L}. \quad (22)$$

When eccentricity oscillations are suppressed at later times, the above equations hold when taking $\bar{\Omega}_{\text{SL}} = \Omega_{\text{SL}}$, $\bar{\Omega}_L = \Omega_L$, and $\bar{I} = I$.

The most convenient coordinate system is the non-inertial one where $\hat{\mathbf{z}} = \hat{\boldsymbol{\Omega}}_e$. In this reference frame, the polar coordinate is just θ_e as defined above in Eq. (27), and the equation of motion becomes

$$\frac{d\hat{\mathbf{S}}}{dt} = \left[\bar{\boldsymbol{\Omega}}_e \hat{\mathbf{z}} + \sum_{N=1}^{\infty} \boldsymbol{\Omega}_{eN} \cos\left(\frac{2\pi Nt}{P_{\text{LK}}}\right)\right] \times \hat{\mathbf{S}} - \dot{I}_e \hat{\mathbf{y}} \times \hat{\mathbf{S}}. \quad (23)$$

If we break $\hat{\mathbf{S}}$ into components $\hat{\mathbf{S}} = S_x \hat{\mathbf{x}} + S_y \hat{\mathbf{y}} + \cos \theta_e \hat{\mathbf{z}}$ and define complex variable

$$S_{\perp} \equiv S_x + iS_y, \quad (24)$$

we can rewrite Eq. 23 as

$$\begin{aligned} \frac{dS_{\perp}}{dt} = & i\bar{\Omega}_e S_{\perp} - \dot{I}_e \cos \theta_e + \sum_{N=1}^{\infty} [\cos(\Delta I_N) S_{\perp} \\ & - i \cos \theta \sin(\Delta I_N)] \Omega_{eN} \cos N\Omega t. \end{aligned} \quad (25)$$

Here, for each Ω_{eN} Fourier harmonic, we denote its magnitude Ω_{eN} and its inclination angle relative to \mathbf{L}_{out} as I_N , using the same convention as Fig. 4, and $\Delta I_N = I_e - I_N$. Finally, $\Omega \equiv 2\pi/T_{\text{LK}}$ is the LK frequency, where T_{LK} is defined as the ω half-period.

3. ANALYSIS: DEVIATION FROM ADIABATICITY

3.1. The Adiabatic Invariant

Since Eq. (23) is difficult to study exactly, we first neglect the $N \geq 1$ harmonic terms for simplicity, yielding equation of motion

$$\left(\frac{d\boldsymbol{\Xi}}{dt}\right)_{\text{rot}} = \bar{\boldsymbol{\Omega}}_e \times \boldsymbol{\Xi}. \quad (26)$$

It is not obvious that analysis of Eq. (26) is applicable to Eq. (18). Empirically, we find that, except for the conditions studied in Section 4, the LK-average of $\hat{\mathbf{S}}$ evolves nearly like Eq. (26). Intuitively, this corresponds to assuming the $N \geq 1$ harmonics vanish when taking the LK-average of Eq. (18) except near resonances; a formal proof is beyond the scope of this paper.

Eq. (26) has one desirable property: θ_e , given by

$$\cos \theta_e \equiv \boldsymbol{\Xi} \cdot \hat{\boldsymbol{\Omega}}_e, \quad (27)$$

is an adiabatic invariant. The adiabaticity condition requires the precession axis evolve slowly compared to the precession frequency at all times:

$$\left|\frac{d\hat{\boldsymbol{\Omega}}_e}{dt}\right| \ll |\hat{\boldsymbol{\Omega}}_e|. \quad (28)$$

Since the orientation of $\bar{\boldsymbol{\Omega}}_e$ changes on timescale t_{GW} , we see that the adiabatic assumption is roughly equivalent to assuming each LK period can be Fourier decomposed [Eq. (18)]. Denoting $\bar{\boldsymbol{\Omega}}_e \equiv |\bar{\boldsymbol{\Omega}}_e|$, the adiabaticity condition can be expressed as

$$\frac{dI_e}{dt} \ll \bar{\Omega}_e. \quad (29)$$

3.2. Calculating Deviation from Adiabaticity

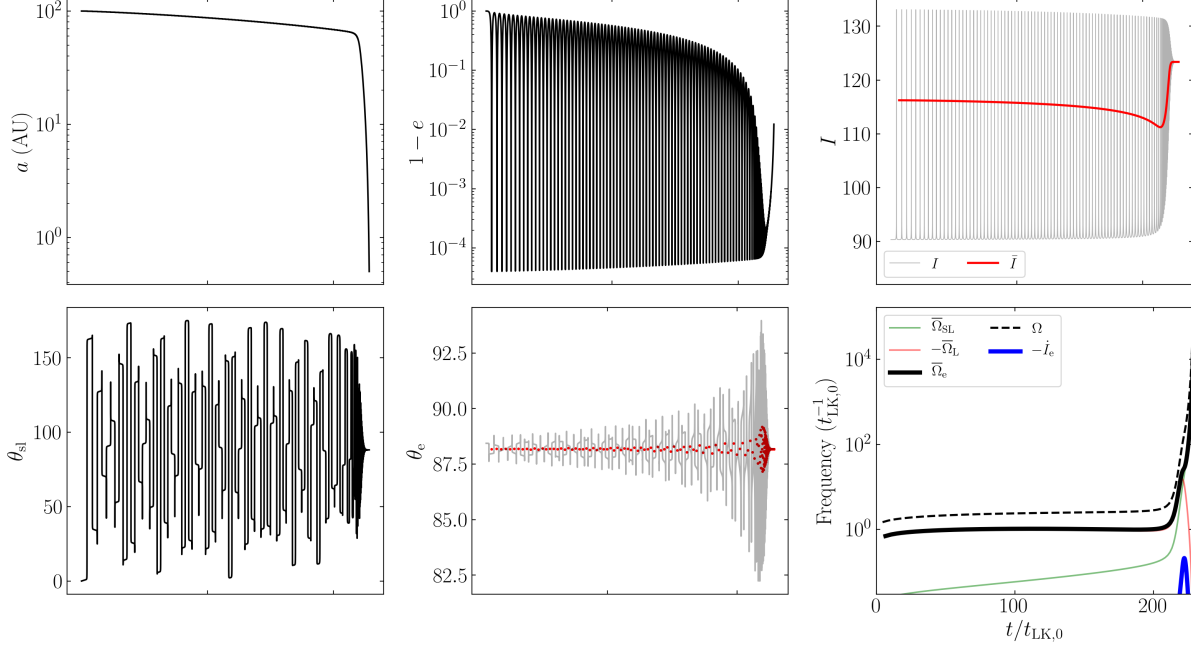


Figure 3. Orbital and spin evolution in a system for which the total change in the adiabatic invariant θ_e is $\lesssim 0.01^\circ$. The inner binary is taken to have $a = 100$ AU, $m_1 = 30M_\odot$, $m_2 = 20M_\odot$, $I_0 = 90.35^\circ$, and $e_0 = 0.001$, while the tertiary SMBH has $\tilde{a}_3 = 2.2$ pc, $m_3 = 3 \times 10^7 M_\odot$. We take $\theta_{sl}^i = 0$. The top three panels a ; e ; and the inclination of the inner binary, both instantaneous (I) and appropriately averaged following Eq. (20) (\bar{I}). The bottom three panels show the instantaneous spin-orbit misalignment angle θ_{sl} ; the angle between $\bar{\Omega}_e$ [Eq. (16)] and both the instantaneous spin vector (light grey) and the LK-averaged spin vector [red dots, denoted θ_e , Eq. (27)]; and four characteristic frequencies of the system [Eqs. 16 and (17)]. The unit of time is the LK timescale [Eq. (7)] evaluated for the initial conditions $t_{LK,0}$.

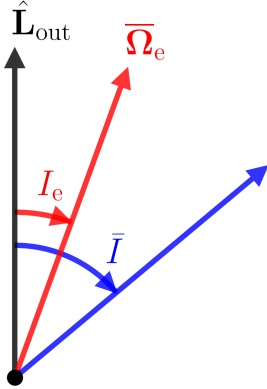


Figure 4. Definition of angles, shown in plane of the two angular momenta \mathbf{L}_{out} and \mathbf{L} , or the $\hat{\mathbf{x}}-\hat{\mathbf{z}}$ plane in the corotating frame. Note that for $I > 90^\circ$, $I_e < 0$.

When neglecting harmonic terms, Eq. (25) becomes

$$\frac{dS_\perp}{dt} = i\bar{\Omega}_e S_\perp - \dot{I}_e \cos \theta_e. \quad (30)$$

This can be solved in closed form using an integrating factor. Defining

$$\Phi(t) \equiv \int^t \bar{\Omega}_e dt, \quad (31)$$

we obtain solution until final time t_f

$$e^{-i\Phi} S_\perp \Big|_{-\infty}^{t_f} = - \int_{-\infty}^{t_f} e^{-i\Phi(\tau)} \dot{I}_e \cos \theta d\tau. \quad (32)$$

It can be seen that, in the adiabatic limit [Eq. (29)], $|S_\perp| = \sin \theta_e$ is conserved over timescales $\gg 1/\bar{\Omega}_e$, as the phase of the integrand in the right hand side varies much faster than the magnitude.

Recalling $|S_\perp| = \sin \theta_e$ and analyzing Eq. (32), we see that $\sin \theta_e \approx \theta_e$ oscillates about its value at $t = -\infty$ with amplitude

$$|\Delta \theta_e| \sim \frac{\dot{I}_e}{\bar{\Omega}_e}. \quad (33)$$

This is compared to the $\Delta \theta_e$ from simulations in the bottom center panels of Figs. 5 and 6 as the green line. We see that in the latter simulation, the faster merger, the order of magnitude of $|\Delta \theta_e|$ is somewhat well predicted, while in the slower merger a second contribution dominates $\Delta \theta_e$ oscillations, discussed in Section 4.

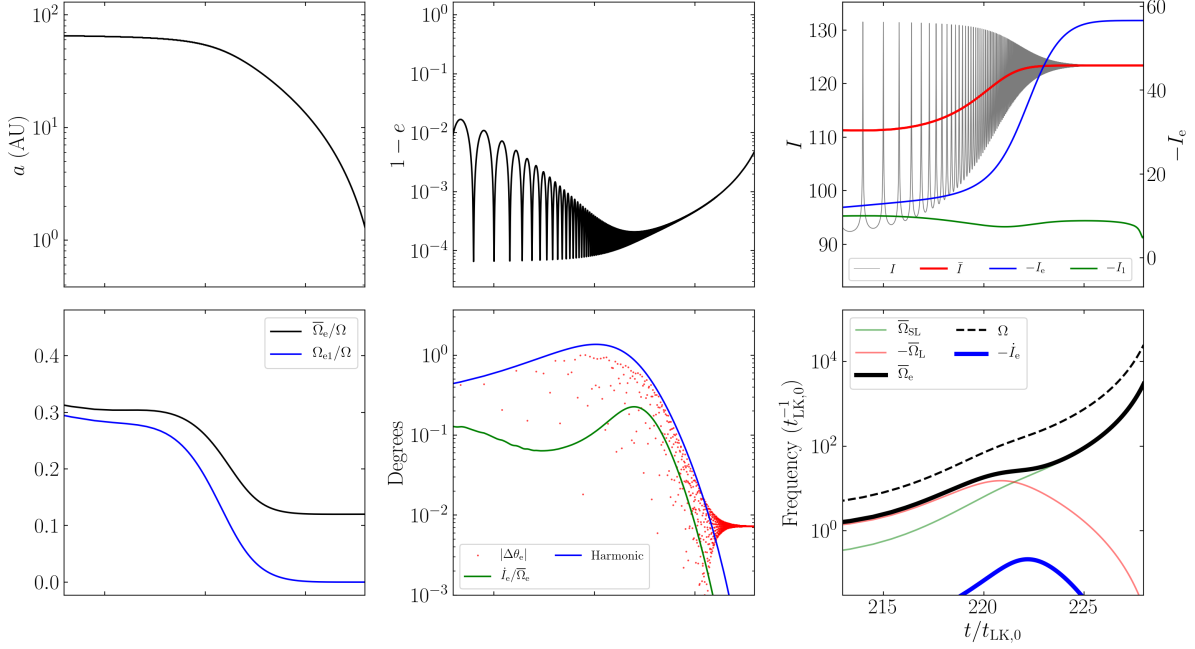


Figure 5. The same simulation as Fig. 3 but shown focusing on the region where $\mathcal{A} \approx 1$. The top three panels depict a , e , I and \bar{I} as before, but in addition I_e [Eq. (21)] and I_l are shown in the third panel. The bottom three panels depict the frequency ratios between the zeroth and first Fourier components of Ω_e to the LK frequency $\Omega = 2\pi/P_{LK}$; the magnitude of oscillation of θ_e away from its initial value (red dots) as well as amplitude estimates due to non-adiabatic effects [green, Eq. (33)] and due to resonances with harmonic terms [blue, Eq. (52)]; and the same characteristic frequencies as before. In the bottom middle panel, it is clear that oscillations in θ_e are dominantly driven by interactions with the $N = 1$ harmonic.

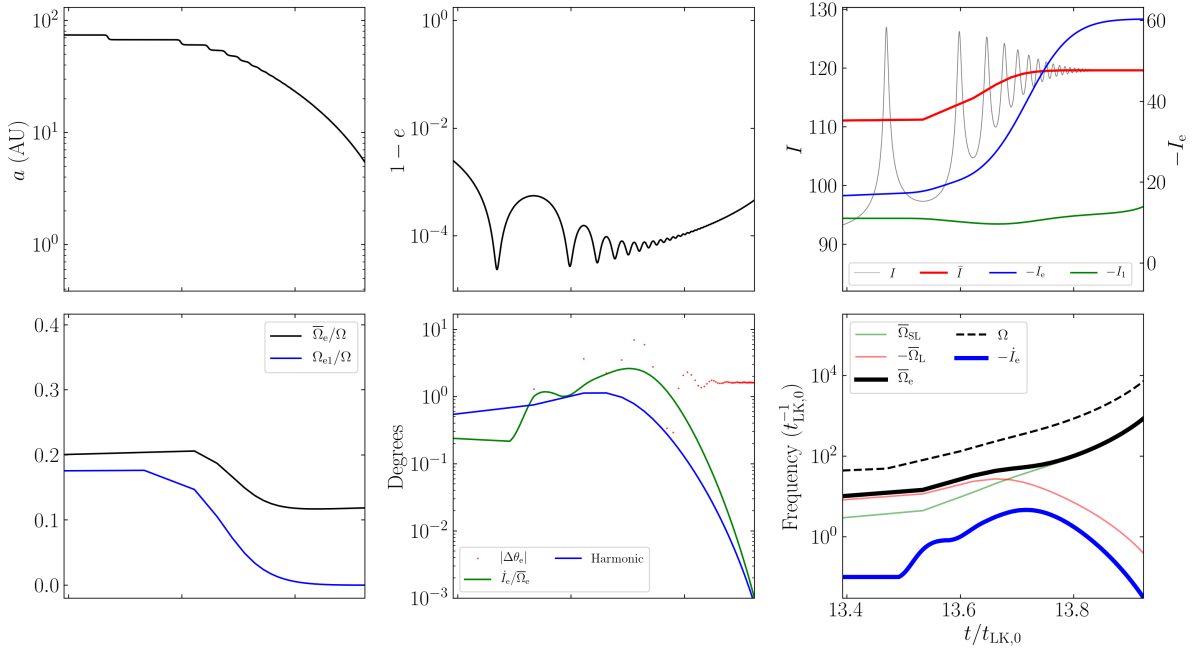


Figure 6. Same as Fig. 5 except for $I_0 = 90.2^\circ$, corresponding to a faster merger and a total change in θ_e of $\approx 2^\circ$. In the bottom middle panel, the nonadiabatic contribution is more significant and causes much poorer conservation of θ_e .

Furthermore, if we denote $|\Delta\theta_e|^f$ to be the total change in θ_e from $t = -\infty$ to merger, we can give loose bound¹

$$|\Delta\theta_e|^f \lesssim \left| \frac{\dot{I}_e}{\bar{\Omega}_e} \right|_{\max}. \quad (34)$$

In the following section, we show that this value can be calculated to good accuracy from initial conditions.

3.3. Estimate of Deviation from Adiabaticity from Initial Conditions

Towards estimating $\left| \dot{I}_e / \bar{\Omega}_e \right|_{\max}$, we first differentiate Eq. (21),

$$\dot{I}_e = \left(\frac{\dot{\mathcal{A}}}{\mathcal{A}} \right) \frac{\mathcal{A} \sin \bar{I}}{1 + 2\mathcal{A} \cos \bar{I} + \mathcal{A}^2}. \quad (35)$$

It also follows from Eq. (16) that

$$\bar{\Omega}_e = \bar{\Omega}_L \left(1 + 2\mathcal{A} \cos \bar{I} + \mathcal{A}^2 \right)^{1/2}, \quad (36)$$

from which we obtain

$$\left| \frac{\dot{I}_e}{\bar{\Omega}_e} \right| = \left| \frac{\dot{\mathcal{A}}}{\mathcal{A}} \right| \frac{1}{\left| \bar{\Omega}_L \right|} \frac{\mathcal{A} \sin \bar{I}}{(1 + 2\mathcal{A} \cos \bar{I} + \mathcal{A}^2)^{3/2}}. \quad (37)$$

This is maximized when $\mathcal{A} \simeq 1$, and so we obtain that the maximum deviation should be bounded by

$$\left| \frac{\dot{I}_e}{\bar{\Omega}_e} \right|_{\max} \simeq \left| \frac{\dot{\mathcal{A}}}{\mathcal{A}} \right| \frac{1}{\left| \bar{\Omega}_L \right|} \frac{\sin \bar{I}}{(2 + 2 \cos \bar{I})^{3/2}}. \quad (38)$$

To evaluate this, we make two assumptions: (i) \bar{I} is approximately constant, and (ii) $j_{\min} = \sqrt{1 - e_{\max}^2}$ evaluated at $\mathcal{A} \simeq 1$ is some constant multiple of the initial j_{\min} , so that

$$j_{\star} \equiv (j)_{\mathcal{A} \simeq 1} = f \sqrt{\frac{5}{3}} \cos^2 I_0, \quad (39)$$

for some unknown factor $f > 1$; we use star subscripts to denote evaluation at $\mathcal{A} \simeq 1$. f turns out to be relatively insensitive to I_0 . This can be as systems with lower e_{\max} values take more cycles to attain $\mathcal{A} \simeq 1$ and thus experience a similar amount of decay due to GW radiation.

For simplicity, let's first assume $\mathcal{A} \simeq 1$ is satisfied when the LK oscillations are mostly suppressed, and $e_{\star} \approx 1$ throughout the LK cycle (we will later see that the scalings are the same

in the LK-oscillating regime). Then we can write

$$\mathcal{A} \simeq \frac{3Gn(m_2 + \mu/3)}{2c^2 a j^2} \left[\frac{3 \cos \bar{I} + 1 + 3e^2/2}{4t_{\text{LK}} j} \right]^{-1}, \quad (40)$$

$$\simeq \frac{G(m_2 + \mu/3)m_{12}\tilde{a}_3^3}{c^2 m_3 a^4 j \cos \bar{I}}, \quad (41)$$

$$\propto \frac{1}{a^4 j}, \quad (42)$$

$$\frac{\dot{\mathcal{A}}}{\mathcal{A}} = -4 \left(\frac{\dot{a}}{a} \right)_{\text{GW}} + \frac{e}{j^2} \left(\frac{de}{dt} \right)_{\text{GW}}. \quad (43)$$

Approximating $e_{\star} \approx 1$ in Eqs. (9) and (10) gives

$$\left[\frac{\dot{\mathcal{A}}}{\mathcal{A}} \right]_{\mathcal{A} \simeq 1} \simeq \frac{64G^3 \mu m_{12}^2}{5c^5 a_{\star}^4 j_{\star}^7} \times 15, \quad (44)$$

$$\bar{\Omega}_{L,\star} \approx \frac{3 \cos \bar{I}}{2t_{\text{LK}} j_{\star}}, \quad (45)$$

$$\left| \frac{\dot{I}_e}{\bar{\Omega}_e} \right|_{\max} \approx \frac{128G^3 \mu m_{12}^2}{c^5 a_{\star}^4 j_{\star}^6} \frac{t_{\text{LK}}}{\cos \bar{I}} \frac{\sin \bar{I}}{(2 + 2 \cos \bar{I})^{3/2}}. \quad (46)$$

With the ansatz for j_{\star} given by Eq. (39) and requiring Eq. (41) equal 1 for a given j_{\star} and a_{\star} gives us the final expression

$$\left| \frac{\dot{I}_e}{\bar{\Omega}_e} \right|_{\max} \approx \frac{128G^3 \mu m_{12}^3 \tilde{a}_3^3}{c^5 \sqrt{Gm_{12}m_3}} \left(\frac{c^2 m_3 \cos \bar{I}}{G(m_2 + \mu/3)m_{12}\tilde{a}_3^3} \right)^{11/8} \times (j_{\star})^{-37/8} \frac{\tan \bar{I}}{(2 + 2 \cos \bar{I})^{3/2}}. \quad (47)$$

The agreement of Eq. (47) with numerical simulation is remarkable, as shown in Fig. 7.

Above, we assumed that $\mathcal{A} \simeq 1$ is satisfied when the eccentricity is mostly constant (see Fig. 3 for an indication of how accurate this is for the parameter space explored in Fig. 7). It is also possible that $\mathcal{A} \simeq 1$ occurs when the eccentricity is still undergoing substantial oscillations. In fact, Eq. (47) is still accurate in this regime when replacing e with e_{\max} , due to the following analysis. When $e_{\min} \ll e_{\max}$, the binary spends a fraction $\sim j_{\min}$ of the LK cycle near $e \simeq e_{\max}$ (Anderson et al. 2016). This fraction of the LK cycle dominates both GW dissipation and $\bar{\Omega}_L$ precession. Thus, both $\dot{\mathcal{A}}$ and $\bar{\Omega}_L$ in Eq. (38) are evaluated at $e \approx e_{\max}$ and are suppressed by a factor of j_{\min} . However, $\dot{\mathcal{A}}$ and $\bar{\Omega}_L$ appear in the numerator and denominator of Eq. (47) respectively, and so the j_{\min} factors cancel. In conclusion, when the eccentricity is still substantially oscillating, Eq. (47) remains accurate when e is replaced with e_{\max} .

The accuracy of Eq. (47) in bounding the total change in $\Delta\theta_e^f$ over inspiral is shown in Fig. 8. Note that conservation of θ_e is generally much better than Eq. (47) predicts; cancellation of phases in Eq. (32) is generally more efficient than Eq. (47) assumes.

¹ Given the complicated evolution of $\bar{\Omega}_e$ and \dot{I}_e , it is difficult to give a more exact bound on the deviation from adiabaticity. In practice, deviations $\lesssim 1^\circ$ are observationally indistinguishable, so the exact scaling in this regime is negligible.

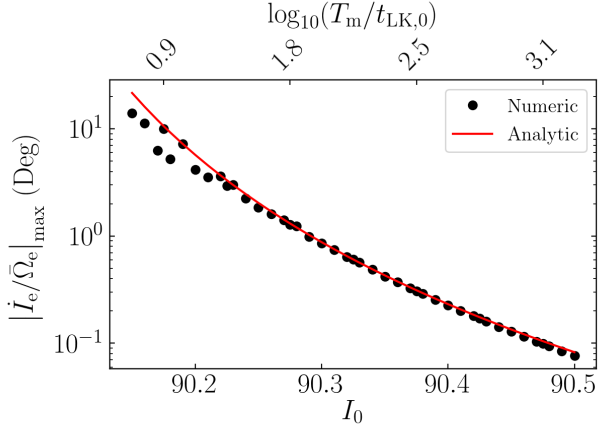


Figure 7. Comparison of $|\dot{e}/\bar{\Omega}_e|_{\max}$ extracted from simulations and using Eq. (47), where we take $f = 2.6$ in Eq. (39). The merger time P_m is shown along the top axis of the plot in units of the characteristic LK timescale at the start of inspiral $t_{LK,0}$; the LK period is initially of order a few $t_{LK,0}$. The agreement is remarkable for mergers that are more adiabatic (towards the right).

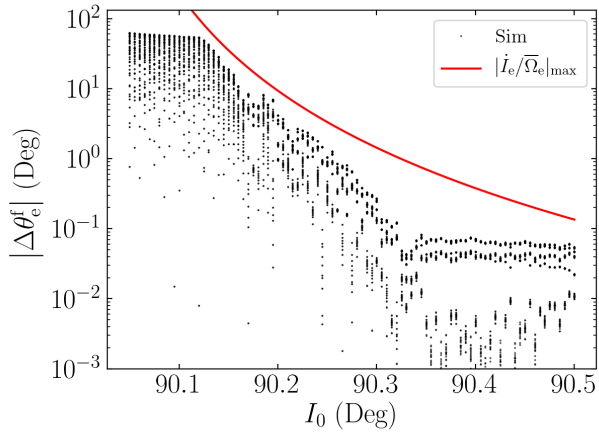


Figure 8. Total change in θ_e over inspiral as a function of initial inclination I_0 , where the initial $\bar{\Omega}_e$ is computed without GW dissipation. For each I_0 , 100 simulations are run for \mathbf{S} on a uniform, isotropic grid. Plotted for comparison is the bound $|\Delta\theta_e^f| \lesssim |\dot{e}/\bar{\Omega}_e|_{\max}$, using the analytical scaling given by Eq. (47). It is clear that the given bound is not tight but provides an upper bound for non-conservation of θ_e due to nonadiabatic effects. At the right of the plot, the accuracy saturates: this is because neglecting GW dissipation causes inaccuracies when computing the average $\bar{\Omega}_e$.

4. ANALYSIS: RESONANCES AND BREAKDOWN OF θ_e CONSERVATION

In the previous section, we neglected the $N \geq 1$ Fourier harmonics in Eq. (23). However, this assumption breaks down near certain resonances described below. For simplicity, we

ignore the effects of GW dissipation in this section and assume the system is exactly periodic (and $\dot{e} = 0$). Eq. (25) is then:

$$\frac{dS_{\perp}}{dt} = i\bar{\Omega}_e S_{\perp} + \sum_{N=1}^{\infty} [\cos(\Delta I_N) S_{\perp} - i \cos \theta \sin(\Delta I_N)] \Omega_{eN} \cos N\Omega t. \quad (48)$$

In this equation, there are potentially resonances when $\bar{\Omega}_e = N\Omega$. Since, $\bar{\Omega}_e \lesssim \Omega$ for most regions of parameter space (see Fig. 10), we restrict our analysis to resonances with the $N = 1$ component. The two possible resonant behaviors are a parametric resonance [modulation of the oscillation frequency in Eq. (48)] and resonant forcing by the second term. Parametric resonances are typically very narrow and are therefore hard to excite as the system's frequencies change under GW dissipation. As such, we consider only the effect of the second term in Eq. (48).

Restricting our attention to $N = 1$ and neglecting the parametric term, the equation of motion reduces to

$$\frac{dS_{\perp}}{dt} \approx i\bar{\Omega}_e S_{\perp} - i \cos \theta_e \sin(\Delta I_1) \Omega_{e1} \cos(N\Omega t). \quad (49)$$

We can approximate $\cos(N\Omega t) \approx e^{iN\Omega t}/2$, as the $e^{-iN\Omega t}$ component is far from resonance. Then we can write down solution

$$\Phi(t) = \int_0^t \bar{\Omega}_e d\tau, \quad (50)$$

$$e^{-i\Phi} S_{\perp} \Big|_{-\infty}^{\infty} = - \int_{-\infty}^{\infty} \frac{i \sin(\Delta I_1) \Omega_{e1}}{2} e^{-i\Phi(\tau) + i\Omega\tau} \cos \theta_e d\tau. \quad (51)$$

Thus, similarly to Section 3.2, $|\Delta\theta_e|$ can be bound by

$$|\Delta\theta_e| \sim \frac{1}{2} \frac{\sin(\Delta I_1) \Omega_{e1}}{|\Omega - \bar{\Omega}_e|}. \quad (52)$$

This is shown as the blue line in the bottom center panels of Fig. 5 and 6. We see that the amplitude of oscillations in θ_e are well described by Eq. (52), particularly in the former case (where the non-adiabatic contribution is weaker).

Again analogously to Section 3.2, we obtain loose bound for total nonconservation of θ_e

$$|\Delta\theta_e|^f \lesssim \left| \frac{\sin(\Delta I_1) \Omega_{e1}}{\Omega - \bar{\Omega}_e} \right|_{\max}. \quad (53)$$

If we assume the right hand side in Eq. (53) is maximized initially, we can predict $\Delta\theta_e^f$ for mildly LK-enhanced mergers (Liu & Lai 2017) rather well, as shown in Fig. 9.

While Eq. (52) depends on the properties of the $N = 1$ Fourier component, the condition for substantial θ_e non-conservation can be understood in terms of physical quantities:

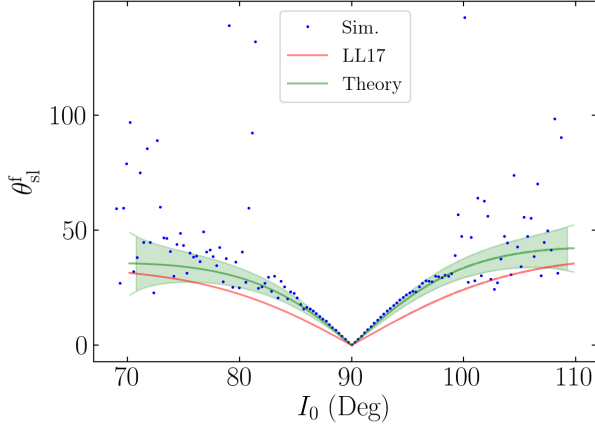


Figure 9. Zoomed in version of Fig. 1 with updated predictions from this work. The green line gives θ_{sl}^f assuming perfect conservation of θ_e , and the green shaded region gives the total expected deviation according to Eq. (52), evaluated for the initial orbital parameters. The further deviation of the simulation results from the predicted width can be understood as the system evolving in such a way that $|\Delta\theta_e|$ is increasing.

- $\sin(\Delta I_1)$ is small unless $\mathcal{A} \approx 1$. Otherwise, Ω_e does not nutate appreciably within an LK cycle, and all the Ω_{eN} are aligned with Ω_e , implying all the $\Delta I_N \approx 0$.
- Smaller values of both e_{\min} and e_{\max} increase $\bar{\Omega}_e/\Omega$, as shown in Fig. 10, strengthening the interaction with the $N = 1$ resonance.

LK-driven coalescence causes \mathcal{A} to increase on a similar timescale to that of e_{\min} increase (see Fig. 3). As such, we conclude that the effect of harmonic terms generally only affects θ_e conservation when $\mathcal{A} \approx 1$ initially.

5. CONCLUSION AND DISCUSSION

Relation between θ_e and θ_{sl}^f , as a function of I .

The “chaotic” behavior in Paper I is because it satisfies the heuristic provided at the end of the harmonics section well.

Interestingly, harmonic terms begin to dominate $\Delta\theta_e$ at quite small inclinations $I_0 \lesssim 90.35^\circ$, but the non-adiabatic contribution to nonconservation obviously dominates out to $I_0 \approx 90.4^\circ$.

REFERENCES

- Anderson, K. R., Storch, N. I., & Lai, D. 2016, Monthly Notices of the Royal Astronomical Society, 456, 3671
- Kozai, Y. 1962, The Astronomical Journal, 67, 591
- Lidov, M. L. 1962, Planetary and Space Science, 9, 719
- Liu, B., & Lai, D. 2017, The Astrophysical Journal Letters, 846, L11
- , 2018, The Astrophysical Journal, 863, 68
- Peters, P. C. 1964, Physical Review, 136, B1224
- Storch, N. I., & Lai, D. 2015, Monthly Notices of the Royal Astronomical Society, 448, 1821

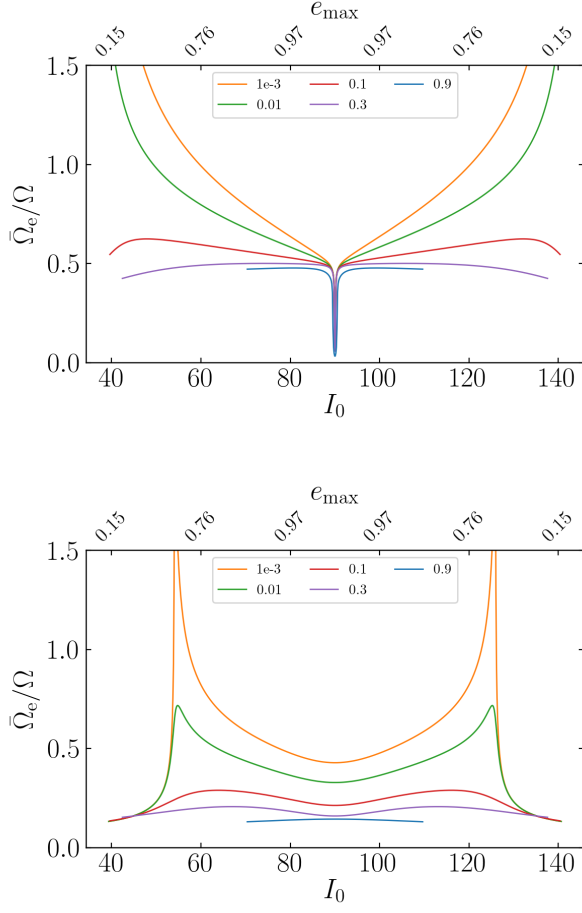


Figure 10. For the fiducial parameters (top) and for the inner parameters (bottom), $\bar{\Omega}_e/\Omega$ as a function of I_0 (corresponding to e_{\max} labeled on top axis) for varying values of e_{\min} . Both smaller e_{\min} and e_{\max} values more easily satisfy the resonant condition $\bar{\Omega}_e/\Omega \approx 1$. Data are only shown when $e_{\min} < e_{\max}$.